Towards establishing a long-term cloud record from space-borne lidar observations

Artem Feofilov
LMD (Laboratoire de Météorologie Dynamique)
Sorbonne Université, UPMC Univ Paris 06, CNRS, École Polytechnique
Paris, France
afeofilo@lmd.ipsl.fr

Hélène Chepfer
LMD (Laboratoire de Météorologie Dynamique)
Sorbonne Université, UPMC Univ Paris 06, CNRS, École Polytechnique
Paris, France
chepfer@lmd.ipsl.fr

Vincent Noël
LAERO (Laboratoire d'Aérologie)
CNRS/UT3, Observatoire Midi-Pyrénées,
Toulouse, France
vincent.noel@aero.obs-mip.fr

Maryam Hajiaghazadeh-Roodsari
LMD (Laboratoire de Météorologie Dynamique)
Sorbonne Université, UPMC Univ Paris 06, CNRS, École Polytechnique
Paris, France
maryam.hajiaghazadeh-roodsari@lmd.ipsl.fr

Abstract
Clouds play a crucial role in the Earth's energy budget, but their feedback is still uncertain. A comprehensive understanding of clouds, including their coverage, vertical distribution, and optical properties, is necessary for comprehension and forecasting the Earth's energy budget and climate. Satellite observations have been providing a continuous monitoring of clouds, with active sounders being of particular importance because of their vertical and horizontal resolution and accuracy. But comparing the clouds retrieved from different space-borne lidars is challenging because of differences in wavelength, pulse energy, detector type, local time of overpass, and so on. This study presents an approach to merge clouds measured by the space-borne lidar ALADIN/Aeolus (355nm), with clouds retrieved from the CALIPSO lidar observations (532nm). The method involves compensating for the instrumental differences to get comparable cloud datasets. This method sets a path for integrating future lidars, such as ATLID/EarthCare, into the global lidar cloud record.

Keywords — clouds, ALADIN, CALIOP, lidar

I. INTRODUCTION

Clouds play an important role in the radiative energy budget of Earth. The radiative effect of clouds is twofold: on the one hand, clouds reflect some of the Sun's radiance during the day, thus preventing surface warming. On the other hand, high thin clouds trap some of the outgoing infrared radiation emitted by the surface and re-emit it back to the ground, thus contributing to its heating. Overall, at global scale, clouds contribute to cool the Earth radiatively, but quantifying precisely this global effect as well as the influence of clouds on the Earth radiative budget everywhere requires knowing the coverage of clouds, as well as their geographical and vertical distributions, temperature, and optical properties.

Satellite observations have been providing a continuous survey of clouds over the whole globe. Among the space-borne sounders, the lidars play a special role because they measure the vertical backscatter radiance profiles with high precision. However, the properties are not the same for any pair of lidar instruments. These differences define the active instruments' capability of detecting atmospheric aerosols and/or clouds for a given atmospheric scenario and observation conditions (day, night, averaging distance). At the same time, there is an obvious need to ensure the continuity of global space-borne measurements and to get a smooth transition between the satellite missions [1][2][3].

In this work, we show the method, which compensates for the wavelength difference, lack of cross-polar channel, and for the diurnal cycle for ALADIN/Aeolus lidar in comparison with CALIOP/CALIPSO lidar. This approach will help to continue the cloud climatology record when the new space-borne lidars become operational.

II. LIDAR DATA USED IN THE STUDY

A. CALIPSO-GOCCP

CALIOP, a two-wavelength polarization-sensitive near nadir viewing lidar, provides high-resolution vertical profiles of aerosols and clouds [4][5][6]. In Tab. 1, we provide the main characteristics of this lidar instrument. The General Circulation Model (GCM) Oriented Cloud Calipso Product (CALIPSO-GOCCP) is derived from CALIPSO L1/NASA products at Laboratory of Dynamic Meteorology (LMD) and Institute of Pierre-Simon Laplace (IPSL) with the support of NASA/CNES, ICARE Thematic Center (Lille, France), and ClimServ data service (IPSL) and it contains observational cloud diagnostics including the instantaneous scattering ratio (profiles) at the native horizontal resolution of CALIOP (333 m) and at 480 m vertical resolution [7][8][9].

B. ALADIN lidar onboard Aeolus satellite

The Aeolus satellite carries a Doppler wind lidar called ALADIN (see the third column in Tab. 3), which operates at 355 nm wavelength and is composed of a transmitter, a Cassegrain telescope, and a receiver capable of separating the molecular (Rayleigh) and particular (Mie) backscattered photons (high spectral resolution lidar, HSRL). Its main purpose is measuring winds, but it also provides information on optical properties of the atmosphere. In this study, we used Aeolus L2A aerosol optical properties product [10].

When using the ALADIN's measured backscattered radiance in the retrieval of atmospheric optical properties, it is crucial to compensate for a loss of perpendicular backscattered component, which is not registered by ALADIN's detectors.

TABLE I.   ALADIN AND CALIOP SPACE-BORNE LIDARS

Parameter\Instrument	CALIOP	ALADIN
Orbit inclination [deg]	98.00	96.97
Orbit height	705→688	320
Equator crossing LT [h]	01:30/13:30	06:00/18:00
Off-nadir angle [deg]	3	35
PRF [Hz]	20.1	50
Native horiz. res. [m]	333	140 (2800)
Native vert. res. [m]	60	250-2000
L2 horiz. res. [m]	333	87000
L2 vert. res. [m]	480	250-2000
Depolarization channel	Yes	No
Wavelength(s) [nm]	532/1064	355
HSRL capacity	No	Yes
Detector type	PMT/APD	A-CCD

C. Collocated dataset

In this work, we used the same collocated dataset as in [11]. As for any collocation, there was a trade-off between the quality of collocation and the number of collocated pairs of profiles. In addition, we had to supplement this tradeoff with a requirement of a representative geographical coverage. Finally, we have chosen the night-time collocations corresponding to Δtime < 6h and Δdist < 1deg. This yielded about 7.7E4 pairs of measurements, which cover both the high-, middle-, and low-latitudes in a representative way.

III. DEFINITIONS

A. Lidar equation

The formalism used in this work was described in [11]. In this section, we repeat only the basic definitions needed for understanding the material presented below. The molecular, particulate, and total components of backscatter will get the indices "mol", "part", and "tot", respectively.

The propagation of laser light through the atmosphere and backwards to the detector is described by the lidar equation:

$$ATB(\lambda,z) = (\beta_{mol}(\lambda,z) + \beta_{part}(\lambda,z)) \times$$
$$\times e^{-2\int_{Z_{sat}}^{z}(\alpha_{mol}(\lambda,z\prime)+\eta\alpha_{part}(\lambda,z\prime))dz\prime} \quad (1)$$

where ATB stands for Attenuated Total Backscatter [m^{-1} sr^{-1}], $\beta_{mol}(\lambda,z)$ and $\beta_{part}(\lambda,z)$ are the wavelength-dependent molecular and particulate backscatter coefficients [m^{-1} sr^{-1}], $\alpha_{mol}(\lambda,z)$ and $\alpha_{part}(\lambda,z)$ are the extinction coefficients [m^{-1}], Z_{sat} is the altitude of the satellite, λ is the wavelength, and η is a multiple scattering coefficient (e.g., [12], [13], [14]).

For the HSRL lidar, one can write similar equations for the attenuated radiance backscattered from atmospheric particles and molecules (APB and AMB), respectively:

$$APB(\lambda,z) = \beta_{part}(\lambda,z) \times e^{-2\int_{Z_{sat}}^{z}(\alpha_{mol}(\lambda,z\prime)+\eta\alpha_{part}(\lambda,z\prime))dz\prime} \quad (2)$$

$$AMB(\lambda,z) = \beta_{mol}(\lambda,z) \times e^{-2\int_{Z_{sat}}^{z}(\alpha_{mol}(\lambda,z\prime)+\eta\alpha_{part}(\lambda,z\prime))dz\prime} \quad (3)$$

For cloud definition, we will also need to define the attenuated molecular backscatter for clear sky conditions

$$ATB_{mol}(\lambda,z) = \beta_{mol}(\lambda,z) \times e^{-2\int_{Z_{sat}}^{z}\alpha_{mol}(\lambda,z\prime)dz\prime} \quad (4)$$

where η stands for the multiple scattering coefficient ([7], [14] [15], [16], [17]).

B. Cloud detection and cloud variables

For the cloud detection, we use the scattering ratio (SR):

$$SR(532nm,z) = \frac{ATB(532nm,z)}{ATB_{mol}(532nm,z)} \quad (5)$$

We declare a layer as cloudy if the following two conditions are met:

$$SR(532nm,z) > 5$$
$$ATB(532nm,z) - ATB_{mol}(532nm,z) > 2.5 \times 10^{-6}\ m^{-1}\ sr^{-1} \quad (6)$$

If a given atmospheric layer was observed multiple times or if it was sampled vertically at several points, we define the cloud fraction profile CF(z) as:

$$CF(z) = \frac{N_{cld}(z)}{N_{tot}(z)} \quad (7)$$

where $N_{cld}(z)$ is the number of times the conditions of Eq. (6) are met and $N_{tot}(z)$ is the total number of measurements in this layer.

IV. METHOD

In this section, we introduce the three corrections required to make the clouds estimated from the Aeolus L2A optical product comparable to clouds retrieved from the CALIOP observations.

A. Wavelength conversion

The condition (6) was used in CALIPSO-GOCCP (e.g. [7], [8], [16], [17]) and we suggest keeping it for other lidars to ensure the consistency between cloud products. In application to ALADIN, this will mean using the recalculated to 532nm values of ATB, which will be estimated from (1), $\beta_{part}(355nm,z)$ and $\alpha_{part}(355nm,z)$ retrieved from the measurements (Eqs. 2 and 3) and $\beta_{mol}(532nm,z)$ and $\alpha_{mol}(532nm,z)$ retrieved or estimated from pressure-temperature profiles from reanalysis. In the numerical experiment below, we calculated $ATB_{mol}(532nm,z) = \beta_{mol}(532nm,z) \times e^{-2\int_{Z_{sat}}^{z}\alpha_{mol}(532,z\prime)dz\prime}$ using the available pressure-temperature profiles and the formalism provided in [11]. Here, we reproduce the Eq. 8 of this paper:

$$SR\prime(532nm,z) =$$
$$= \frac{(\beta_{mol}(532,z)+\beta_{part}(355,z)) \times e^{-2\int_{Z_{sat}}^{z}(\alpha_{mol}(532,z\prime)+\eta_{355}\alpha_{part}(355,z\prime))dz\prime}}{\beta_{mol}(532,z) \times e^{-2\int_{Z_{sat}}^{z}\alpha_{mol}(532,z\prime)dz\prime}} \quad (8)$$

B. Compensation for missing depolarized component

The formalism and cloud definition outlined above imply that for a given atmospheric volume, the backscattered radiance represents the total number of backscattering molecules and particles, and this has a clear physical meaning – the higher the concentration of backscattering particles, the thicker the cloud. However, the design of ALADIN does not allow measuring the perpendicular backscatter. This creates a serious obstacle for merging the cloud records from two satellites: either we must change the definition of the cloud and compare only parallel backscatter component, or we have to compensate for the missing perpendicular radiance. Since the former approach changes the definition of the cloud and makes the cloud product incomparable to previous results, we have to propose a method of the total signal recovery from the

existing data. For this, we used the depolarized signal statistics available from the CALIOP.

To compensate for the missing depolarized component, we tested several schemes: the climatological correction, the look-up-table (LUT) correction, and the neural network parameterization approach. The first one is the most straightforward one and at the same time it yields more consistent results than the other two, so we present it here. Using 5 years of the nighttime CALIOP data, we have built the monthly climatology over the latitudes and heights (Fig.1).
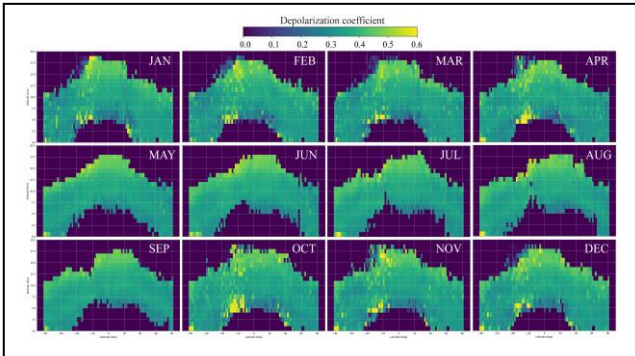
Fig. 1. Depolarization coefficient climatology built from the nighttime CALIPSO data collected in 2016-2020.
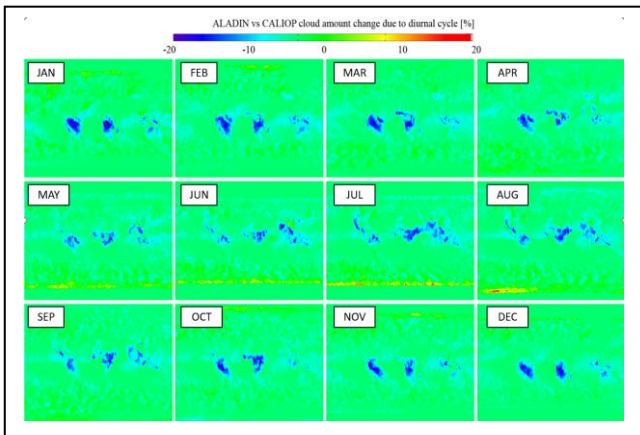

Fig. 2. Diurnal cycle correction for ALADIN clouds w.r.t. CALIOP clouds estimated from AIRS/IASI. Only high clouds (P<440 hPa) are considered.
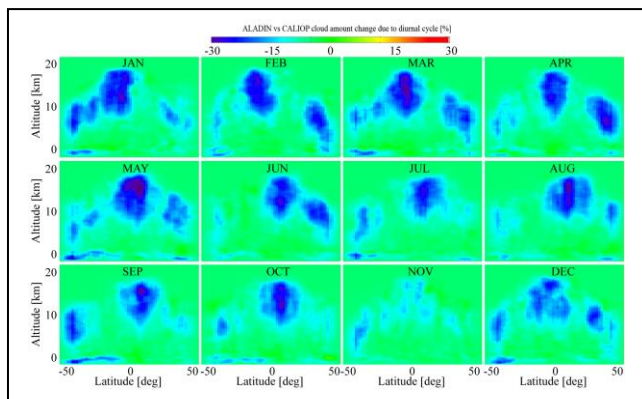

Fig. 3. Diurnal cycle correction for ALADIN clouds w.r.t. CALIOP clouds estimated from CATS. Note the difference in format (altitude vs latitude), in color scale, and in the latitude limits, compared to Fig. 2.

C. Compensation for the difference in overpass time

As mentioned above, the two lidars do not overfly the same area at the same local solar time (LST). CALIOP crosses the equator at 01:30 and 13:30 LST, whereas for Aeolus these times are 06:30 and 18:30 LST. Based on the previous studies [18], [19], [20], [21], and [22], one can say that the cloud diurnal cycle is strong for the high tropical clouds and for low-level clouds over the ocean, reaching 20% in certain areas. In addition, the phase of diurnal cycle is not the same for all clouds. Therefore, there is an obvious need to know the diurnal cycle parameters at all heights and locations to compare the Aeolus clouds with CALIPSO clouds properly.

a) Diurnal cycle correction retrieved from AIRS/IASI observations: These two instruments are passive remote sensors observing the Earth at 01:30 and 13:30 LST and 09:30 and 21:30 LST, respectively. The clouds from these two instruments are retrieved by the CIRS cloud property retrieval package [23], [24]. Applying the diurnal cycle retrieval method outlined in [22], we got the correction shown in Fig. 2.

b) Diurnal cycle correction retrieved from CATS observations: Cloud-Aerosol Transport System (CATS) lidar [25] on the International Space Station (ISS) was operating for more than 2.5 years. We used a gridded monthly dataset, which is a by-product of [20] and passed it through the diurnal cycle retrieval algorithm of [22]. The resulting correction is shown in Fig. 3.

As one can see in Fig. 2 and Fig. 3, the change due to diurnal cycle can reach 30% in cloud cover. The major effects are consistent between two diurnal cycle correction datasets, with the high tropical clouds affected he most, but since the CATS-derived correction provides vertically resolved structure, we use it in the results shown below.

D. Application to collocated dataset and fine-tuning

We applied the corrections described above to the collocated dataset, each time checking the correlation coefficient between the CALIOP and ALADIN cloud products, as well as the overall bias and root-mean-square of the error. In Fig. 4, we show the most important steps from this study: (Fig. 4b) demonstrates a strong underestimation of high clouds if we blindly apply the detection criteria given by Eq. 6; Fig. 4c shows the sensitivity of high cloud detection to ΔATB threshold; Fig. 4d shows the importance of depolarization coefficient correction, Fig. 4e shows further improvement of the agreement when the diurnal cycle correction from CATS is applied (AIRS/IASI correction gives slightly worse results since it accounts only for high-level clouds, and we do not show it here); finally, Fig. 4f shows the cloud amount after the fine-tuning. The latter procedure is allowed in our case because the noise characteristics and sensitivity of the two instruments are not the same, and the conversion procedures applied in the steps A-C do not compensate for these differences. We found that for the baseline 2A12 of the L2A dataset used in the collocated data analysis (2019-2020), the best agreement is achieved for SR>4.5 and $\Delta ATB>7 \times 10^{-7}$ m^{-1} sr^{-1}. These numbers will be likely updated when the latest baseline of Aeolus L2A will be applied to the entire period of ALADIN observations.
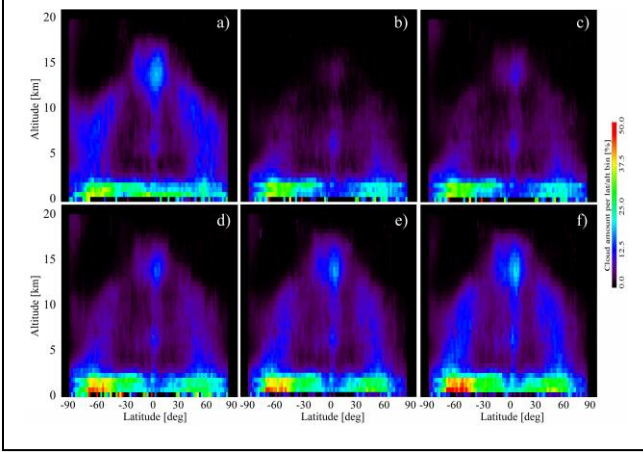
Fig. 4. Latitude/altitude cloud fraction: a) CALIOP reference nighttime data; b) ALADIN with SR>5 and ΔATB $> 2.5 \cdot 10^{-6}$ m^{-1} sr^{-1}; c) ALADIN with SR>5 and ΔATB > 0; d) same as "c", but with the compensation for depolarization using climatological data; e) same as "d", but with diurnal cycle estimated from CATS; f) fine tuning, same as "e", but with SR>4.5 and ΔATB $> 7 \cdot 10^{-7}$ m^{-1} sr^{-1}.

V. RESULTS

A. Total cloud amount

We begin the analysis with the total cloud amount comparison, which we define on the 2°x2° gridded maps as follows: for any given period and for any longitude/latitude grid box, we consider the maximal cloud fraction in the column per month and average these maximal values over the considered period (3 winter months, or 3 summer months, or the whole year). As one can see in Fig. 5, the major cloud features visible in CALIOP cloud plots are well reproduced in ALADIN panels. The differences between the two instruments shown in the bottom row reach ±20%, but they do not have an obvious pattern linked to the cloud system or type. The average differences between the cloud cover vary from −0.5±8% for DJF through 1±12% for JJA to −2±5% for the whole year. It is interesting to note that in 2019 the SAA zone corresponds to a red blob visible over South America in DJF column both for CALIOP and ALADIN. On the difference plots in the bottom row, this zone tends to be negative (blue), indicating that the SAA might have stronger effects on the CALIOP measurements than on the ALADIN.
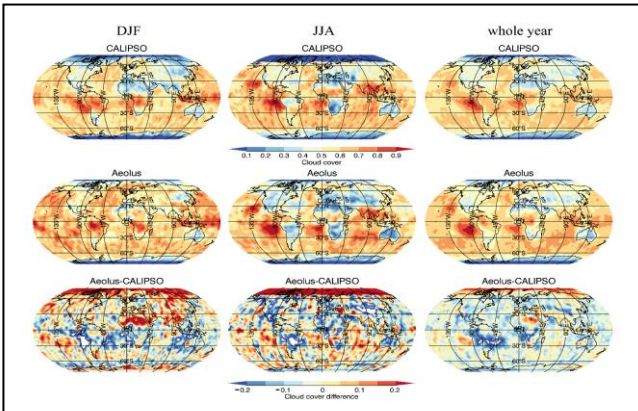

Fig. 5. The total cloud amounts for CALIOP (top), ALADIN (middle), and their difference (bottom) for winter (DJF, left column), summer (JJA, middle column), and for the whole year (right column). Negative bias of CALIOP in the polar zone is due to day/night splitting of orbits and should not be considered as real.

B. Height-stratified cloud amount

In Fig. 6 and 7, we show the DJF and JJA cloud fraction distributions per altitude layer. The heights of 15 km, 8 km, and 3 km have been selected after studying the vertical distributions of cloud fraction for each latitude zone. It is interesting to note a good agreement for high tropical clouds (Fig. 6ab and Fig. 7ab) whereas the middle-level clouds show certain differences at high latitudes (Fig. 6cd and Fig. 7cd). The cloud fraction in the SAA zone on all the panels is always higher for CALIOP, confirming the conclusions made in the previous section. The fine structure of the compared panels is never the same for the same pixel, but the overall agreement is good.
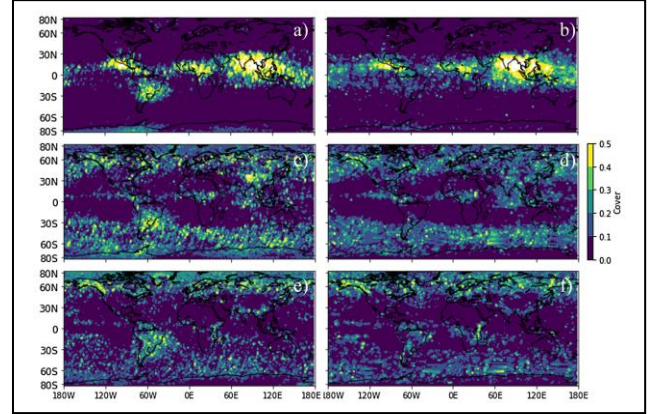

Fig. 6. DJF cloud fraction distribution for high-, middle- and low-level clouds in 2020: (a,b) 15km, (c,d) 8km, (e,f) 3km. Left-hand-side panels: CALIOP, right-hand-side panels: ALADIN.
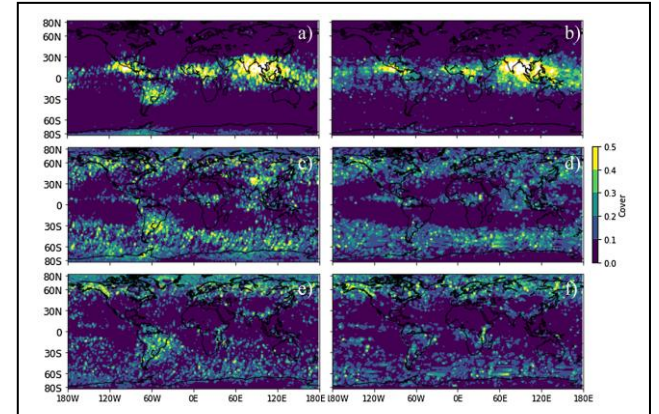

Fig. 7. Same as Fig. 6, but for JJA.

C. Seasonal cycle of cloud amount for specific climate regimes

For this test, we adapted the zones defined in Cloud Assessment Report [26]. The following comparisons give an idea how the different data sets agree in specific regions, corresponding to typical climate regimes. The ten regions of [26] redefined as the circles of 7.5° and 10° radius, are shown on the map in Fig. 8. Regions 1 and 2 correspond to regions with marine boundary layer clouds of small spatial variability in cloud optical depth (COD); ocean storm tracks (with moderate spatial COD variability) can be found in regions 3, 4 and 5; regions 6 and 7 are regions with tropical cirrus with moderate to large spatial COD variability; regions 8 and 9 correspond to regions with active tropical convection with large spatial COD variability; and region 10 gives an example of midlatitude land with clouds of large spatial variability in COD.

For these regions, we have calculated the average cloud fraction in the layers within ±0.5 km of the height corresponding to a peak of cloud height histogram for a given zone (about 1km for zones 1−6, about 14km for zones 7−9, and 1−9 km for zone 10) and plotted them in the corresponding panels of Fig. 9. The average values of seasonal cycle in zones 1 and 2 are close to each other, but the correlation coefficient is moderate, whereas for other zones the time series of cloud fractions retrieved from two lidars overlap pretty well, yielding the correlation coefficient values up to 0.93 for midlatitude land clouds of zone 10.
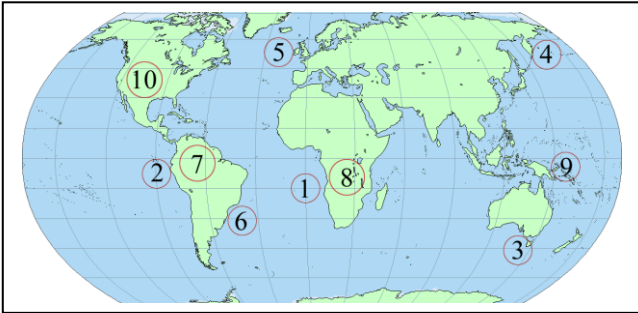

Fig. 8. Geographical map of specific regions of typical cloud regimes [26]: (1) SH Str Africa, (2) SH Str America, (3) SH midlatitude storm, (4) NH storm Eastern Pacific, (5) N Atlantic storm, (6) SH Ci off America, (7) SH Ci Amazon, (8) SH Cb Africa, (9) NH Cb Indonesia, (10) ARM Southern Great Plain.
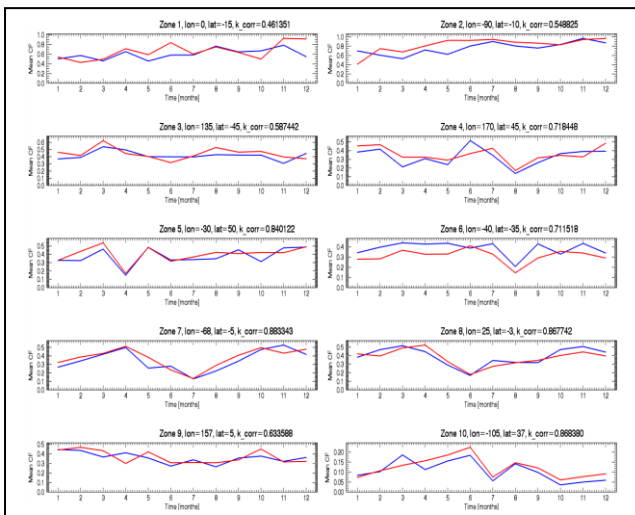

Fig. 9. Seasonal cycle for the zones defined in Fig. 8. Blue lines: CALIOP, red lines: ALADIN.

D. Time series for zonal mean vertical cloud profiles

Last, but not least, we have built the monthly average cloud fraction per latitude zone over the whole analyzed period of 2006−2023, see Fig. 10. Knowing the potential difficulty of the comparison in the SAA zone, we excluded the area that might be affected by the SAA, which we define as ($-90 < \text{lon} < 30$; $-60 < \text{lat} < 0$). In the panels of Fig. 10, a single column represents one month of data, and the dark line at the beginning of 2016 corresponds to one month missing from CALIOP data. To imitate the "cloud climatology", which would be created if the CALIPSO was de-orbited before the launch of Aeolus, we use CALIOP data before September 2018 and then switch to ALADIN. To illustrate the problem of different baselines in the present Aeolus L2A data, we overlaid the panels with a red line showing the transitions between the baselines (bottom of the line corresponds to

baseline 2A12 whereas the uppermost point corresponds to baseline 2A16). As one can see, in a number of cases noticeable transitions in Fig. 10 correspond to the baseline change: 2A15 to 2A12 in the middle of 2019 for the upper 4 panels, 2A12 to 2A13 in the middle of 2021 for the top and bottom panels, 2A13 to 2A14 at the beginning of 2022 for almost all panels, 2A14 for 2A15 at the end of 2022 for almost all panels. These observations raise an important question regarding self-consistent reprocessing of the whole 2A dataset each time the baseline changes. To our knowledge, the Aeolus team plans such a reprocessing in the beginning of 2024. With the new dataset, the optimization of cloud detection described above will be repeated, and the updated thresholds will be applied to a new self-consistent data set.

Before this update happens, one could propose to use a set of variable thresholds to compensate for the baseline change, but this will be a sort of masking one problem with the tweaking at another stage, and the correction will be purely ad hoc, so we do not recommend this kind of fixing unless absolutely necessary.
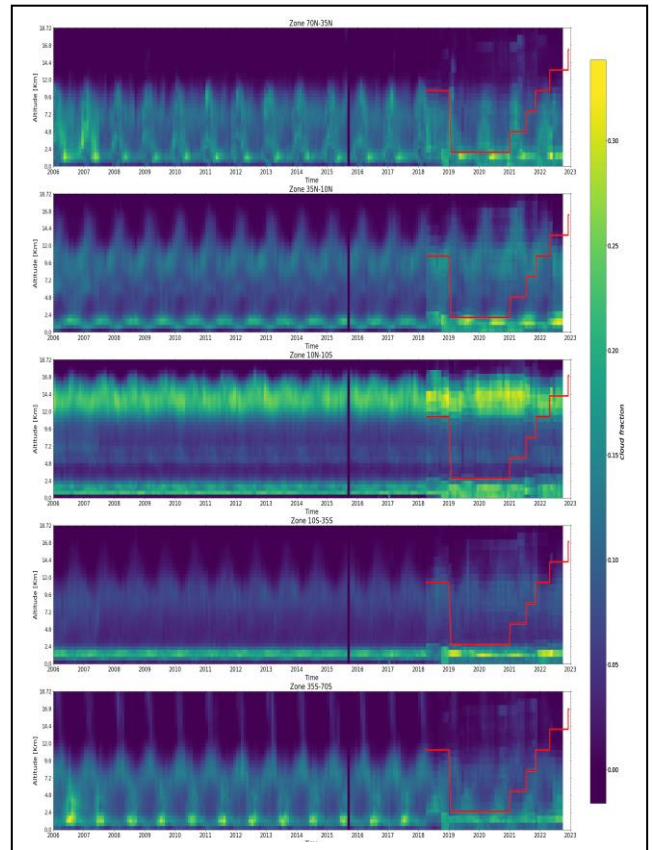

Fig. 10. Altitude-time series for the combination of CALIOP clouds (June 2006−August 2018) and ALADIN clouds (September 2018−now) for different latitude zones. The SAA region was excluded. The red lines in the right-hand side of each panel correspond to the baseline change, from 2A12 (the bottom line) to 2A16 (near the end of observation period).

VI. CONCLUSIONS

For a pair of completely different lidar instruments, CALIOP and ALADIN, we have developed a method of compensating for (a) wavelength, (b) lack of depolarization, (c) cloud diurnal cycle, and (d) differences in noise levels. With these corrections, we have produced and analyzed the joint CALIOP-ALADIN cloud dataset for the period of June 2006 – March 2023. The analysis shows that (i) the CALIOP

is probably more prone to SAA anomaly effects than ALADIN, (ii) global cloud amount demonstrates similar behavior in all seasons with the mean difference of about −2±5% that is within the initially defined limits for this work, (iii) the height-stratified geographical distributions are close to each other, (iv) the seasonal cycle of mean cloud fraction in 10 different zones corresponding to specific cloud regimes is coherent between the datasets with Pearsons' correlation coefficients reaching the values of 0.8-0.9. However, we need to stress that the time series of cloud fraction vertical distribution for the zonal mean shows a signature of the 2A baseline shift, indicating the need of 2A reprocessing with the single baseline and in a coherent manner.

Overall, the method developed in this work demonstrated the expected results, and its key elements will be transferred to merging the clouds estimated from the future ATLID/EarthCare spaceborne lidar observations. The difficulties associated with the recovery of missed cross-polar component indicate the importance of using the cross-polar channel in future lidar instruments.

VII. Acknowledgements

VIII. References

[1] Winker, D., Chepfer, H., Noël, V., and Cai, X.: Observational constraints on cloud feedbacks: The role of active satellite sensors. Surveys in Geophysics, 38, 1483−1508, https://doi.org/10.1007/s10712-017-9452-0, 2017.

[2] Chepfer, H., Noël, V., Winker, D., and Chiriaco, M.: Where and when will we observe cloud changes due to climate warming?, Geophys. Res. Lett., 41, 8387–8395, doi:10.1002/2014GL061792, 2014.

[3] Chepfer H., Noël, V., Chiriaco, M., Wielicki, B., Winker, D., Loeb, N., and Wood, R.: The potential of multi-decades space-born lidar to constrain cloud feedbacks, J. Geophys. Res. Atmos., DOI:10.1002/2017JD027742, 2018.

[4] Winker, D. M., Hunt, W. H., and Hostetler, C. A.: Status and Performance of the CALIOP Lidar, Proc. SPIE vol 5575, 8-15, 2004.

[5] Winker, D. M., Hunt, W. H., and McGill, M. J.: Initial performance assessment of CALIOP, Geophys. Res. Lett., 34, L19803, doi:10.1029/2007GL030135, 2007.

[6] Winker, D. M., Vaughan, M. A., Omar, A. H., Hu, Y., Powell, K. A., Liu, Z., Hunt, W. H., and Young, S. A.: Overview of the CALIPSO Mission and CALIOP Data Processing Algorithms, J. Atmos. Ocean. Tech., 26, 2310–2323, doi:10.1175/2009JTECHA1281.1, 2009.

[7] Chepfer H., Bony, S., Winker, D., Chiriaco, M., Dufresne, J.-L., Sèze, G.: Use of CALIPSO lidar observations to evaluate the cloudiness simulated by a climate model, Geophys. Res. Let., 35, L15704, doi:10.1029/2008GL034207, 2008.

[8] Chepfer H., Bony, S., Winker, D., Cesana,G., Dufresne, J.-L., Minnis, P., Stubenrauch, C. J., and Zeng, S.: The GCM Oriented Calipso Cloud Product (CALIPSO-GOCCP). J. Geophys. Res., 115, D00H16, doi:10.1029/2009JD012251, 2010.

[9] Chepfer H., Cesana, G., Winker, D., Getzewich, B., Vaughan, M., and Liu, Z.: Comparison of two different cloud climatologies derived from CALIOP attenuated backscattered measurements (Level 1): the CALIPSO-ST and the CALIPSO-GOCCP. J. Atmos. Oceanic Technol., doi: 10.1175/JTECH-D-12-00057.1, 2012.

[10] Flament, T., Trapon, D., Lacour, A., Dabas, A., Ehlers, F., and Huber, D.: Aeolus L2A aerosol optical properties product: standard correct algorithm and Mie correct algorithm, Atmos. Meas. Tech., 14, 7851–7871, https://doi.org/10.5194/amt-14-7851-2021, 2021.

[11] Feofilov, A. G., H. Chepfer, V. Noël, R. Guzman, C. Gindre, P.-L. Ma, and M. Chiriaco: Comparison of scattering ratio profiles retrieved from ALADIN/Aeolus and CALIOP/CALIPSO observations and preliminary estimates of cloud fraction profiles. Atmos. Meas. Tech., 15, 1055–1074, https://doi.org/10.5194/amt-15-1055-2022, 2022.

[12] Platt, C. M. R.: Lidar and radiometric observations of cirrus clouds, J. Atmos. Sci. 30, 1191–1204, 1973.

[13] Garnier, A., Pelon, J., Vaughan, M. A., Winker, D. M., Trepte, C. R., and Dubuisson, P.: Lidar multiple scattering factors inferred from CALIPSO lidar and IIR retrievals of semi-transparent cirrus cloud optical depths over oceans, Atmos. Meas. Tech., 8(7), 2759–2774, https://doi.org/10.5194/amt-8-2759-2015, 2015.

[14] Donovan, D. P.: The Expected Impact of Multiple Scattering on ATLID Signals, EPJ Conf., 119(1), 01006, doi: 10.1051/epjconf/201611901006, 2016.

[15] Chiriaco, M., Vautard, R., Chepfer, H., Haeffelin, M., Dudhia, J., Wanherdrick, Y., Morille, Y., and Protat, A.: The Ability of MM5 to Simulate Ice Clouds: Systematic Comparison between Simulated and Measured Fluxes and Lidar/Radar Profiles at the SIRTA Atmospheric Observatory, Monthly Weather Rev., 134(3), 897−918, https://doi.org/10.1175/MWR3102.1, 2006.

[16] Chepfer H., Cesana, G., Winker, D., Getzewich, B., and Vaughan, M.: Comparison of two different cloud climatologies derived from CALIOP Level 1 observations: the CALIPSO-ST and the CALIPSO-GOCCP, J. Atmos. Ocean. Tech., 30(4), 725−744 doi.10.1175/JTECH-D-12-00057.1, 2013.

[17] Reverdy M., Chepfer, H., Donovan, D., Noël, V., Cesana, G., Hoareau, C., Chiriaco, M., Bastin, S.: An EarthCARE/ATLID simulator to evaluate cloud description in climate models, J. Geophys. Res. Atmos., 120(21), 11090−11113, doi: 10.1002/2015JD023919, 2015.

[18] Cairns, B.: Diurnal variations of cloud from ISCCP data. Atmos. Res., 37, 133-146, doi: 10.1016/0169-8095(94)00074-N, 1995.

[19] Rossow, W. B., and Cairns, B.: Monitoring changes of clouds. Climatic Change, 31, 175–217, doi: 10.1007/BF01095151, 1995.

[20] Noel, V., Chepfer, H., Chiriaco, M., and Yorks, J.: The diurnal cycle of cloud profiles over land and ocean between 51° S and 51° N, seen by the CATS spaceborne lidar from the International Space Station, Atmos. Chem. Phys., 18, 9457–9473, doi: 10.5194/acp-18-9457-2018, 2018.

[21] Chepfer, H.; Brogniez, H. and Noel, V., Diurnal variations of cloud and relative humidity profiles across the tropics Scientific Reports, 9, 16045, https://doi.org/10.1038/s41598-019-52437-6, 2019.

[22] Feofilov, A. G. and Stubenrauch, C. J.: Diurnal variation of high-level clouds from the synergy of AIRS and IASI space-borne infrared sounders, Atmos. Chem. Phys., 19, 13957–13972, https://doi.org/10.5194/acp-19-13957-2019, 2019.

[23] Feofilov, A. and Stubenrauch, C.: LMD Cloud Retrieval using IR sounders. Algorithm Theoretical Basis, CIRS-LMD software package V2, 19 pp., doi: 10.13140/RG.2.2.15812.63361, 2017.

[24] Stubenrauch, C. J., Feofilov, A. G., Protopapadaki, E.-S., and Armante, R.: Cloud climatologies from the InfraRed Sounders AIRS and IASI: Strengths and Applications, Atmos. Chem. Phys., 17, 13625-13644, doi: 10.5194/acp-17-13625-2017, 2017.

[25] McGill, M. J., Yorks, J. E., Scott, V. S., Kupchock, A. W., and Selmer, P. A.: The Cloud-Aerosol Transport System (CATS): A technology demonstration on the International Space Station, Proc. Spie., 9612, doi:10.1117/12.2190841, 2015.

[26] Stubenrauch, C. J., and 22 Coauthors: Assessment of global cloud datasets from satellites: Project and database initiated by the GEWEX radiation panel, Bull. Am. Meteorol. Soc., 94(7), 1031–1049, doi:10.1175/BAMS-D-12-00117.1, 2013.